Journal of Hazardous Materials 399 (2020) 123097

Contents lists available at ScienceDirect

Journal of Hazardous Materials

journal homepage: www.elsevier.com/locate/jhazmat

3D printed photoreactor with immobilized graphitic carbon nitride: A sustainable platform for solar water purification

Qinmin Zheng[a], Ashlee Aiello[b], Yoon Sil Choi[a,1], Kayla Tarr[a,1], Hongchen Shen[a], David P. Durkin[b,*], Danmeng Shuai[a,*]

[a] Department of Civil and Environmental Engineering, The George Washington University, Washington, DC 20052, United States
[b] Department of Chemistry, United States Naval Academy, Annapolis, MD 21402, United States

GRAPHICAL ABSTRACT

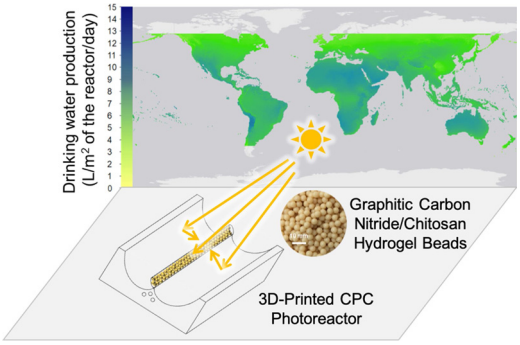

ARTICLE INFO

Editor: Daniel C.W. Tsang

Keywords:
Graphitic carbon nitride
Chitosan hydrogel
Photocatalytic reactor
Micropollutant removal

ABSTRACT

Solar-energy-enabled photocatalysis is promising for sustainable water purification. However, photoreactor design, especially immobilizing nano-sized photocatalysts, remains a major barrier preventing industrial-scale application of photocatalysis. In this study, we immobilized photocatalytic graphitic carbon nitride on chitosan to produce g-C_3N_4/chitosan hydrogel beads (GCHBs), and evaluated GCHB photoreactivity for degrading phenol and emerging persistent micropollutants in a 3D printed compound parabolic collector (CPC) reactor. The CPC photocatalytic system showed comparable performance with slurry reactors for sulfamethoxazole and carbamazepine degradation under simulated sunlight, and it maintained the performance for contaminant removal in real water samples collected from water/wastewater treatment plants or under outdoor sunlight irradiation. Global drinking water production was estimated for the CPC system, and it holds promise for small-scale sustainable water treatment, including, but not limited to, the production of high-quality potable water for single houses, small communities, rural areas, and areas impacted by natural disasters in both developed and developing countries.

* Corresponding authors.
E-mail addresses: durkin@usna.edu (D.P. Durkin), danmengshuai@gwu.edu (D. Shuai).
[1] These authors contribute equally.

https://doi.org/10.1016/j.jhazmat.2020.123097
Received 19 January 2020; Received in revised form 26 May 2020; Accepted 30 May 2020
Available online 05 June 2020
0304-3894/

1. Introduction

Solar-energy-enabled photocatalysis is a sustainable advanced oxidation process (AOP) which can utilize renewable energy to oxidize organic micropollutants, inactivate pathogens, and eradicate biofilms from drinking water and wastewater (Hoffmann et al., 1995; Chong et al., 2010; Miranda-García et al., 2011; Keane et al., 2014; Raulio et al., 2006). It is a promising technology for small-scale water purification, especially for highly cost-sensitive and energy-restrictive areas (Loeb et al., 2018). Despite substantial research over the past few decades, the practical application of photocatalysis in water treatment systems has been very limited due to low photocatalytic efficiency and high cost of photocatalyst and reactor development, operation, and maintenance. TiO_2 is the most widely explored photocatalyst for pilot- or industrial-scale photocatalytic reactor applications, due to its low cost, high abundancy, and robustness (Chong et al., 2010; Keane et al., 2014; Braham and Harris, 2009). A large number of surface functional groups on TiO_2 also allow easy and diverse immobilization of the photocatalyst into reactors. One major challenge of using TiO_2 for photocatalytic water treatment is its limited performance under visible light irradiation that prevents the harvest and use of a larger amount of solar energy (i.e., TiO_2 can only harvest 4% of solar energy in principle). Another challenge is much reduced photocatalytic performance in complex water matrices. The main oxidants produced in TiO_2-based systems are hydroxyl radicals ($O^{\cdot}H$), which degrade most organics non-selectively at a high reaction rate (second-order reaction rate constants of 10^6–10^{10} M^{-1} s^{-1}) (Haag and Yao, 1992; Neta and Dorfman, 1968). However, the non-selectivity of $O^{\cdot}H$ also limits practical applications of TiO_2, because the $O^{\cdot}H$ reactivity for contaminant degradation can be significantly compromised by the presence of natural organic matter (NOM) or other natural water constituents (e.g., carbonate) (Benotti et al., 2009; Brame et al., 2014, 2015; Antoniou et al., 2016).

Recently, graphitic carbon nitride (g-C_3N_4) has emerged as an innovative photocatalyst with several advantages for practical applications in water treatment. For example, most g-C_3N_4 can absorb visible light (with a wavelength shorter than 460 nm), enabling harvest of 13 % of solar energy (Zheng et al., 2017). In addition, g-C_3N_4 is a low-cost material that can be developed from earth abundant precursors, and it exhibits high chemical and thermal stability and biocompatibility (Zheng et al., 2017; Cao et al., 2015; Ong et al., 2016; Dong et al., 2018; Xiao et al., 2017). More importantly, in previous studies, g-C_3N_4 with different compositions (i.e., dopants) has shown high robustness for photocatalytic contaminant degradation, with limited inhibition of contaminant degradation kinetics in complex water matrices due to the generation of more selective reactive species (e.g. $^1O_2$, $O_2^{-\cdot}$, holes) other than nonselective radicals ($O^{\cdot}H$) (Zheng et al., 2016, 2019). However, to the best of our knowledge, very few studies have demonstrated the practicality of using g-C_3N_4 in a photoreactor design for water purification (Moreira et al., 2019). Therefore, in this study, we aim to develop an efficient, sustainable, low-cost, and potentially scalable g-C_3N_4-based photoreactor for water treatment.

Many photoreactors had been designed, including concentrating collectors (e.g. parabolic-trough collector (PTC)) reactor, non-concentrating collector (e.g. inclined plate collector (IPC)) reactor, and compound parabolic collector (CPC) reactors for solar water treatment. (Braham and Harris, 2009) Among these designs, CPC reactors combine the characteristics and advantages of the other two types of reactors. While CPC reactors can concentrate solar radiation with a less collection area, it also retains the simplicity for fabrication. Thus CPC reactor is believed to be the most suitable for pilot-scale or industrial-scale water treatment applications (treatment capacity up to > 1000 L day^{-1}) (Miranda-García et al., 2011; Keane et al., 2014; Braham and Harris, 2009; Spasiano et al., 2015; Sichel et al., 2007; Navntoft et al., 2006; Blanco et al., 1999; Polo-López et al., 2010). However, most CPC reactors use metals in fabrication, and their manufacturing requires high standards and special equipment and instruments. Constructing compound parabolic reflectors with an optimized geometry for collecting solar irradiation needs precise dimensions. Therefore, scalable and low-cost manufacturing of CPC reactors could be challenging, especially for developing countries and economically disadvantaged communities. Additive manufacturing, such as 3D printing, has emerged as a valuable tool that is promising for fabricating CPC reactors. 3D printing not only fabricates the reactors with a well-controlled dimension (with a Z resolution of 25–100 μm), but also enables scalable and low-cost production from plastics (e.g., polylactic acid, acrylonitrile butadiene styrene), and the technology is affordable to people and communities with limited resources. Therefore, we adopted 3D printing for fabricating the CPC reactor in this study.

Besides the selection and fabrication of photoreactors, another challenge of photocatalysis for water purification is photocatalyst immobilization in the reactors. Slurry reactors, operated by suspending micro- or nano-sized g-C_3N_4 particles in the flow-through reactor, can have high reaction kinetics due to enhanced mass transfer rates. However, the main barrier of using slurry reactors is the post-separation of g-C_3N_4 fine particles from the treated water. The immobilization of g-C_3N_4 on hydrogel (Hu et al., 2019; Jiang et al., 2016; Sun et al., 2017; Zhang et al., 2016), Al_2O_3 ceramic foam (Dong et al., 2014), and glass rings (Moreira et al., 2019) for water and air purification have been studied. In this study, we applied chitosan hydrogel beads as a support to immobilize g-C_3N_4 particles. Chitosan is an earth-abundant biopolymer derived from natural chitin, and it has excellent transparency and absorbs a negligible amount of ultraviolet and visible sunlight (only absorbing photons with a wavelength < 200 nm) (Kumirska et al., 2010). Therefore, sunlight can penetrate into GCHBs with little-to-no loss and activate photocatalysis. In addition, chitosan is rich in surface functional groups that can form hydrogen bonds with water, thus capable of forming hydrogels with a high water content (> 90 wt%). Chitosan hydrogels show a 3D interconnected porous structure, with large pore sizes and high porosity, and they can promote reactant mass transfer inside the beads. To date, the studies of g-C_3N_4/chitosan composites for photocatalysis are very limited (Zhao et al., 2018). Our work is unique and innovative because (i) we immobilized g-C_3N_4 into chitosan hydrogel beads and tested photocatalytic performance for degrading persistent organic micropollutants, and (ii) we used 3D printed photoreactors to understand the robustness, scalability, and practicality of immobilized g-C_3N_4 for solar water treatment.

2. Experimental section

2.1. Synthesis of hydrogel beads

The list of reagents and the detailed synthesis procedure of hydrogel beads are provided in the supplementary data (SD). Briefly, the pure chitosan hydrogel beads (CHBs) were sythesized via the coagualtion of chitosan in NaOH solution and subsequent crosslinking with epicholorodydrin (ECH) (Yu et al., 2008). ECH was selected as the crosslinker because it reacts with both amine groups and hydroxyl groups in chitosan, improving the structural stability and mechanical robustness of the coagulated hydrogel (Yu et al., 2008; Chiou and Li, 2003). GCHBs were fabricated via a similar precudure of CHBs synthesis, with the coagulation of a g-C_3N_4-chitosan mixture instead of pure chitosan (Scheme 1). The g-C_3N_4-chitosan mixture was prepared by sufficiently mixing a certain amount of g-C_3N_4 (i.e. $MCB_{0.07}$, synthesized from melamine, cyanucric acid, and babituric acid based on our previous study (Zheng et al., 2016)) and chitosan in acetic acid.

2.2. Hydrogel bead characterization

Scanning electron microscopy (SEM) were used to characterize the morphology of hydrogel beads. The surface area and porosity were determined by liquid N_2 adsorption. The functional groups were analyzed by attenuated total reflectance-Fourier transform infrared

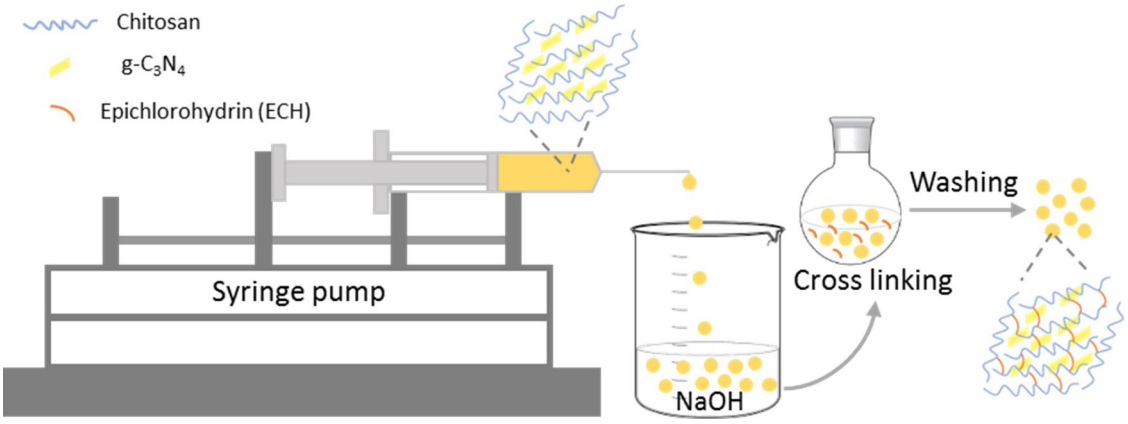

Scheme 1. Synthesis of g-C_3N_4/chitosan hydrogel beads (GCHBs).

spectroscopy (ATR-FTIR). The thermal stability of the synthesized beads was evaluated by thermogravimetic (TG) analysis. The crystal phase was determined by X-ray powder diffraction (XRD). Details of instrumental characterization are provided in the SD.

2.3. CPC reactor design

The CPC reactor (Fig. 1a) mainly comprised two components, a reflector for collecting and distributing the light, and a quartz tube packed with GCHBs for photocatalytic reactions. The reflector of the CPC reactor was fabricated by 3D printing, and its geometry was optimized according to previous studies to allow effective light harvesting and uniform light distribution on the quartz tube (Colina-Márquez et al., 2009, 2010). Reflective aluminum tape was then adhered to the 3D printed reflector. The quartz tube (inner and outer diameter of 20 and 25 mm, respectively) was packed with GCHBs, and it was placed in the center of the CPC reflector. Details of reactor design is provided in the SD.

2.4. Photocatalytic activity test

Photocatalytic contaminant degradation was tested in a 3-inch CPC reactor packed with GCHBs under simulated sunlight (1000 W xenon lamp with an AM 1.5 G optical filter), as shown in Fig. 1b, and a phosphate buffer (1 mM, pH 7.3) containing the contaminant (initial concentration of 100 μM) recirculated through the photoreactor with a flow rate of 50 mL min^{-1} to reduce mass transfer limitations. A higher concentration of contaminants was selected in photocatalysis compared to their environmental concentrations (ng-μg L^{-1}) to facilitate instrumental quantification. A certain amount of GCHBs was packed into the reactor to maintain the g-C_3N_4 loading to the reaction solution of 0.1 g L^{-1}. The photocatalytic contaminant degradation in a slurry reactor with the same g-C_3N_4 photocatalyst powder (0.1 g L^{-1} $MCB_{0.07}$) was conducted for the comparison of degradation kinetics.

The outdoor experiments were conducted in a 12-inch CPC reactor (Fig. 1c) under natural sunlight on The George Washington University campus, with sky conditions ranging from clear to partly cloudy (11:00 − 17:00, Jun 24th, 2019). 300 mL of phosphate buffer (1 mM, pH 7.3) containing phenol (initial concentration of 100 μM) was circulated through a peristaltic water pump to the photoreactor with a flow rate of 50 mL min^{-1}. A certain amount of GCHBs was packed into the reactor to maintain the g-C_3N_4 loading to the reaction solution of 0.2 g L^{-1}.

To explore the influence of water matrices representative of water treatment systems, the reactivity of CPC reactor for phenol degradation under simulated sunlight irradiation was explored in real water samples collected from the Broad Run Wastewater Reclamation Facility (BRWRF, for wastewater treatment and reuse) and Trap Rock Water Treatment Facility (TRWTF, for drinking water treatment), both in VA. The treatment processes of BRWRF and TRWTF are included in the SD (Fig. S3), and water quality parameters are reported in Table S3.

The concentration of contaminants collected at regular time intervals was analyzed by high performance liquid chromatography (HPLC). The light irradiances from 200 − 460 nm for different reactors were recorded by a spectroradiometer. The pseudo-first-order rate constants (k) for contaminant photocatalytic degradation were obtained by

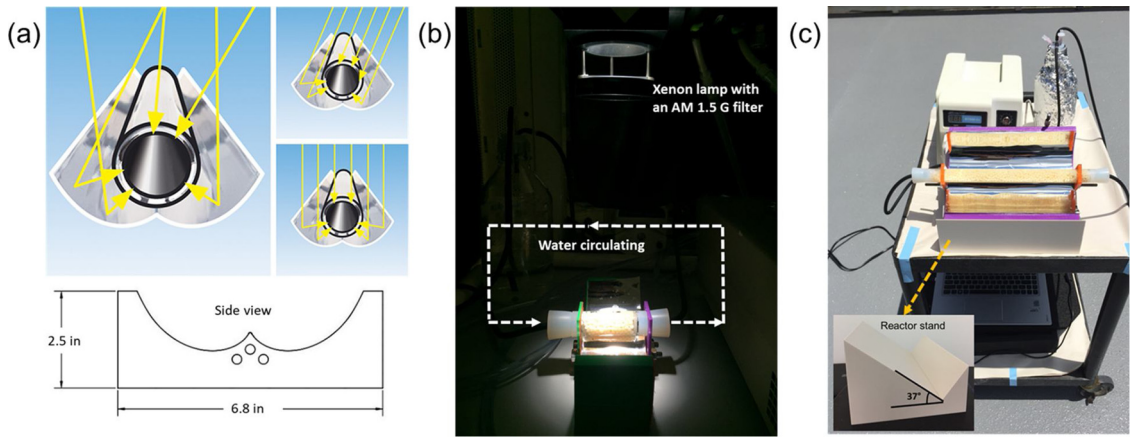

Fig. 1. (a) Side-view and dimension of the 3D printed compound parabolic collector (CPC) reactor (modified from http://www.solfex.co.uk/). Experimental setup for photocatalytic contaminant degradation under (b) simulated sunlight irradiation in the laboratory (3-inch CPC reactor) and (c) outdoor sunlight irradiation (12-inch CPC reactor).

performing a linear regression of natural log of contaminant concentrations versus time (Table S2). The reaction rate constants with 95 % confidence intervals were reported with respect to the light power (200 − 460 nm) and catalyst loading, i.e., the pseudo-first-order rate constant divided by the light power and catalyst loading, which allow the comparison between different reactor configurations and contaminants. Details of the experimental procedures are included in the SD.

2.5. Global map of water production in CPC reactors

The global map of drinking water production volume was created based on the contaminant degradation kinetics (pseudo-first-order reaction rate constants (k), Table S2) in both 3-inch and 12-inch CPC reactors. The drinking water produced at various geographic locations per surface area of the reactor per day, α, (L (m^2 of reactor)$^{-1}$ d^{-1}), can be estimated by the Eq. (1):

$$\alpha = \frac{GHI\,(kWh\,m^{-2}\,d^{-1})}{E\,(kWh)} \times V'(L) \quad (1)$$

where $E(kWh) = I(kW\,m^{-2}) \times S(m^2) \times t(h)$, t is the time needed to achieve 90 % contaminant degradation ($t = \frac{\ln(10)}{k}/60$ (h)), I is the light irradiance for the reactor (integrated from 200 − 4000 nm), S is the surface area of the reactor under light irradiation (Table S2), and V' is the volume of water treated in the reactors (0.15 and 0.3 L for 3-inch and 12-inch reactors, respectively). Global horizontal irradiance (GHI) data at 30 ″ resolution between 60 °N and 45 °S were taken from the Global Solar Atlas. Latitudes outside this range are not available due to satellite imagery accuracy limitations. The map was created using Esri ArcMap software. The photocatalytic reactivity of the CPC reactors was assumed to increase linearly with the increase of sunlight intensity for estimating global drinking water production.

3. Results and discussion

3.1. Optimization of GCHBs synthesis

The bead size and g-C_3N_4 loading of GCHBs were optimized using phenol degradation kinetics as a performance indicator (see details in the SD). Two different sized GCHBs (1.5 and 3 mm in diameter) were fabricated by using 18 and 20 G syringe needles, respectively. In addition, different g-C_3N_4 loadings (5 and 10 wt% of g-C_3N_4 to chitosan) were also prepared and evaluated. CHBs were transparent or semi-transparent, but GCHBs turned yellow with the increase of g-C_3N_4 loading (g-C_3N_4 powder is intrinsically yellow, Fig. 2a). Phenol degradation kinetics indicated GCHBs with 3 mm diameter and 5 wt% of g-C_3N_4 loading had the best performance (Fig. 2b), but the reaction rate constant was not significantly different compared to GCHBs with other sizes and mass loadings of g-C_3N_4 (12–30 % increase of the reaction rate constant). Smaller beads with higher surface curvature and a larger surface area appear to favor photon scattering over absorption, whereas larger beads result in a high free volume between the beads for water flow and a corresponding reduced mass transfer rate. Hence, an optimum bead size should exist. Our results indicate an optimal quartz-tube to bead (diameter) ratio of ca. 6.7 in the limited experimental range investigated, in agreement with a previous study by Ramos, et al. (Ramos et al., 2019) It suggests that desired photon harvesting and mass transfer in the photoreactor was achieved. Increase of the g-C_3N_4 mass loading did not translate into increased photocatalytic activity, likely due to the decrease of light penetration into the reactor and all photons have been harvested and used for photocatalysis.

3.2. Characterization of hydrogel beads

The syntheiszed CHBs and GCHBs both showed good mechanical stability during handling and testing, and negligible destruction of the beads was observed after photocatalysis. Enhanced mechanical stability was attributed to ECH crosslinking. Scanning electron microscopy (SEM) showed both CHBs and GCHBs had a 3D interconnected porous structure, with macropores around 500 nm (Fig. 3a and b). Similar to CHBs, the GCHBs also exihibited macropores, albeit covered with g-C_3N_4, demonstrating the successful embedment of photocatalyst into the chitosan matrix. The surface area and porosity of CHBs and GCHBs before and after photocatalysis were characterized by N_2 gas adsorption. The measured adsorption isotherms and pore size distribution (Fig. 3d and e) indicate that these beads contained mesopores with ~30 % surface microporosity. CHBs had a slightly higher surface area and a larger pore volume than that of GCHBs (64.6 vs. 56.4 $m^2\,g^{-1}$ and 0.145 vs. 0.127 $cm^3\,g^{-1}$), indicating that addition of g-C_3N_4 sacrificed the surface area and porosity of the chitosan hydrogel to some extent (Table 1). This reduction of surface area and porosity in GCHBs was also supported by the SEM characterization. After 6 h photocatalysis, the GCHBs did not show any noticeable changes in surface area or porosity (Table 1), and SEM images indicate their surface morphology was similar (Fig. 3c). These data demostrate that GCHBs are robust in chemical reactions and that chitosan is a suitable support for g-C_3N_4 immoblizaton.

The attenuated total reflectance-Fourier transform infrared spectra (ATR-FTIR) of the CHBs and GCHBs are presented in Fig. 4a. These data are dominated by spectral features of the biopolymer support; strong broad bands extending from 3300 − 3500 cm^{-1} (−OH and −NH−− stretches), 1030 cm^{-1} (C−O stretch) and a series of peaks from 1300 to 1650 cm^{-1} (CN− heterocycle stretching vibrations) clearly indicate the presence of unaltered chitosan (Kumirska et al., 2010). The addition of g-C_3N_4 did not introduce new spectral features, mainly due to the low loading (5 wt%) of g-C_3N_4 in the chitosan beads. In addition, g-C_3N_4 and chitosan have similar functional groups (e.g., N−H, $-NH_2$, or CN−), and thus it might be difficult to discern them by ATR-FTIR.

To further confirm the immoblization of g-C_3N_4 on chitosan, the XRD was conducted for the CHBs and GCHBs. As shown in Fig. S1, CHBs have a specific microcrystalline stucture with two distinct peaks at 9.5° and 20.6° (Zhao et al., 2018). Two characteristic peaks at 13.2° and 27.5° are observed for g-C_3N_4, corresponding to the (002) and (100) diffraction of the g-C_3N_4 structure (Zheng et al., 2016). GCHBs show the chitosan characteristic peaks along with small peaks at 27.5° – the strongest intensity for g-C_3N_4, indicating that g-C_3N_4 were successfully imobilized on chitosan. No significant change of the XRD for GCHBs after the photocatalytic experiments also indicates the structural stability of GCHBs.

Thermogravimetic (TG) analysis evaluated the thermal stability of the synthesized beads, providing insight into long-term robustness of our photocatalytic support. Fig. 4b shows the thermograms (TG) and derivative thermograms (DTG) of g-C_3N_4, CHBs, and GCHBs (fresh and after 6 h photocatalysis). After ca. 260 °C, major weight loss was observed for both CHBs and GCHBs, which was due to the chitosan decomposition (Zhao et al., 2018; Hong et al., 2007). The thermal stability of chitosan up to 260 °C could indicate long-term stability of the bead matrix during solar irradiation. The weight loss of GCHBs after 500 °C is due to the decompostion of g-C_3N_4, and only a small peak was observed in the derivative thermogravimetric analysis (DTGA) because of a low loading of g-C_3N_4 in the GCHBs (Fig. 4c). Pure g-C_3N_4 also started to decompose at 500 °C, which is in agreement with the previous study (Niu et al., 2012). There was also no noticeable difference between fresh GCHBs and GCHBs after 6 h photocatalysis in TGA or DTGA results, indicating the robustness of GCHBs.

3.3. Photocatalytic performance under simulated sunlight irradiation

To evaluate photocatalytic performance, contaminant degradation was first tested in the 3-inch CPC reactor packed with GCHBs (bead diameter of 3 mm, g-C_3N_4 mass loading of 5 wt %) and CHBs (bead

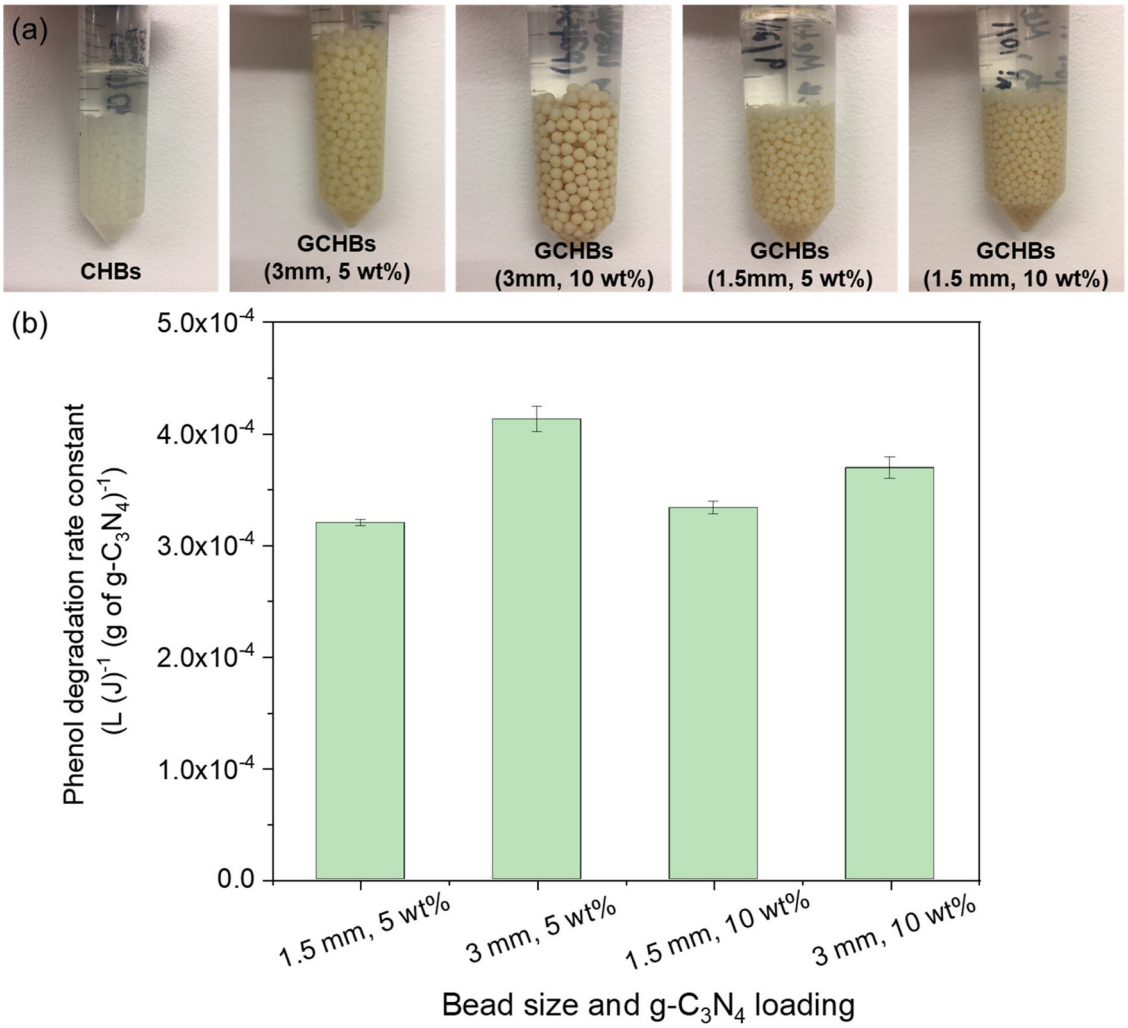

Fig. 2. (a) Photos of CHBs and GCHBs with different properties. (b) Phenol degradation rate constants in a 3-inch CPC reactor packed with GCHBs of different properties under simulated sunlight irradiation (1000 W xenon lamp with an AM 1.5 G optical filter). The initial contaminant concentration was 100 μM, and the reactions were conducted in a phosphate buffer (pH 7.3, 1 mM). Error bars represent 95 % confidence intervals derived from regression analysis of a single run.

diameter of 3 mm, as a control) (Fig. 1b). The reaction kinetics were also compared with that in a slurry reactor with the same g-C_3N_4 photocatalyst powder (as described in our previous study (Zheng et al., 2016)). The slurry reactor was directly placed under the beam to harvest sufficient photons for photocatalysis, and the mixing rate was optimized to eliminate mass transfer limitation in the reaction. The slurry reactor always showed a higher reactivity compared to many flow-through photoreactors because of an optimum configuration in previous research (McCullagh et al., 2011), and the photocatalytic reactivity in the slurry reactor is used as a benchmark to understand the performance of our CPC reactor. Phenol, a widely used surrogate, and persistent organic micropollutants, including atrazine (a herbicide), sulfamethoxazole (SMZ, an antibiotic), and carbamazepine (CBZ, an anticonvulsant) were selected for photocatalytic reactions. The persistent organic micropollutants were used because they are well-known to be recalcitrant to traditional water and wastewater treatment, widely present in natural and treated water, and pose health risks even at very low concentrations (ng-μg L^{-1}) (Oulton et al., 2010). Details of the experimental procedures are included in the SD.

No apparent photocatalytic degradation of contaminants was observed in the control experiment with CHBs (Fig. S2), indicating that pure chitosan beads were not photoreactive. As shown in Fig. 5a, the slurry reactor outperforms CPC reactor for all contaminant's degradation. The largest difference of the photocatalytic activity between the two reactors was observed for atrazine degradation: atrazine degradation was ca. 42-times slower in the CPC reactor than the slurry reactor (1.0×10^{-2} vs. 2.4×10^{-4} L $(J)^{-1}$ (g of g-$C_3N_4)^{-1}$). For phenol, SMZ, and CBZ degradation kinetics, the CPC reactor was 13.1-, 5.4-, and 2.1-times slower than the slurry reactor (5.4×10^{-3} vs. 4.1×10^{-4} L $(J)^{-1}$ (g of g-$C_3N_4)^{-1}$ for phenol, 3.5×10^{-3} vs. 6.4×10^{-4} L $(J)^{-1}$ (g of g-$C_3N_4)^{-1}$ for SMZ and 6.6×10^{-4} vs. 3.1×10^{-4} L $(J)^{-1}$ (g of g-$C_3N_4)^{-1}$ for CBZ), respectively. Chitosan was slightly negatively charged in our experimental setup (pK_a 6.5 vs. pH 7.3 of reaction solution), and it was not expected to interact strongly with neutral contaminants in the reaction solution through electrostatic attraction (pK_as of phenol, atrazine, SMZ, and CBZ are 10.0, 1.7, 1.4/5.8, 2.3/13.9, respectively) (Zheng et al., 2016). The hydrophobicity or hydrophilicity of contaminants and their interactions with hydrophilic chitosan also cannot explain the observed photoactivity among contaminants: log K_{ow} of atrazine, phenol, SMZ, and CBZ are 2.61, 1.46, 0.89, and 2.45, respectively (Hoekman et al., 1995; Dal Pozzo et al., 1989).

One possible explanation of the observed different performance between the CPC reactor and the slurry reactor is the slow mass transfer rate of contaminants inside chitosan hydrogel beads compared to the slurry reactor. Though the beads have a large amount of macropores, the significant amount of micro- and mesoporosity present could reduce the mass transfer rate of reactants. Due to the large size of the beads (ca. 3 mm), the mass transfer can be more seriously inhibited. Atrazine and

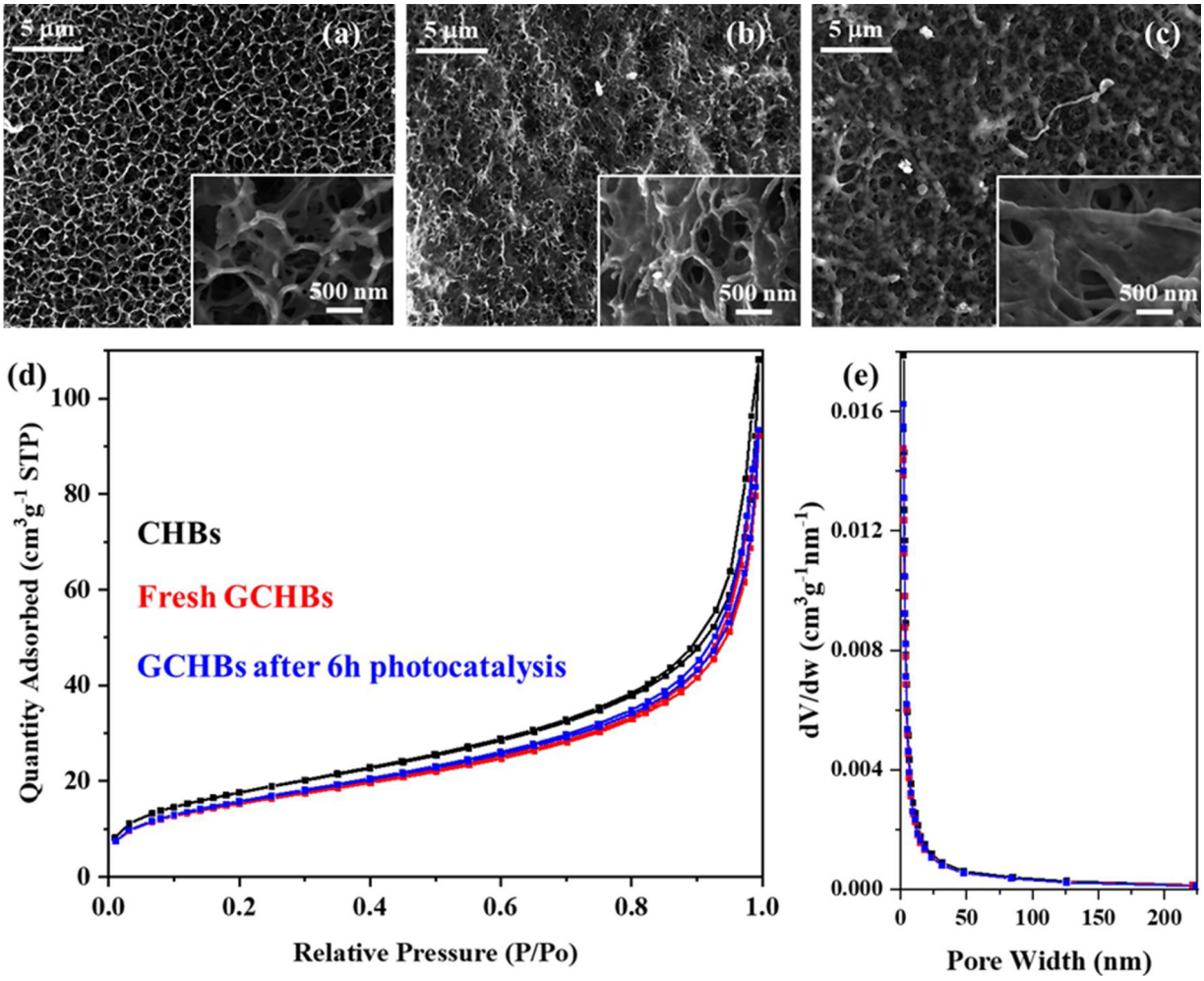

Fig. 3. Scanning electron microscopy (SEM) of (a) CHBs, (b) fresh GCHBs, and (c) GCHBs after 6 h photocatalysis. Low resolution images are presented in the main frames, and higher resolution images of the surface are presented in each inset. (d) N_2 adsorption/desorption isotherms and (e) pore size distribution (calculated using BJH model) of CHBs, fresh GCHBs, and GCHBs after 6 h photocatalysis. The data were collected on samples whose structures were preserved by lyophilization.

Table 1
Summary of liquid N_2 adsorption analysis of CHBs, fresh GCHBs, and GCHBs after 6 h photocatalysis. Standard deviation of duplicates is reported.

Sample	BET surface area ($m^2\ g^{-1}$)	Average pore diameter (nm)	Micropore area ($m^2\ g^{-1}$)	External surface area ($m^2\ g^{-1}$)
CHBs	64.6 ± 0.3	9.11 ± 0.09	16.0 ± 0.2	48.6 ± 0.5
Fresh GCHBs	56.4 ± 0.0	8.95 ± 0.00	13.6 ± 0.1	42.8 ± 0.0
GCHBs after 6 h photocatalysis	58.4 ± 0.3	8.90 ± 0.05	13.6 ± 0.2	44.8 ± 0.1

phenol had a much faster degradation rate compared to that of SMZ and CBZ in slurry reactor, thus their reactivity in the CPC reactor was more likely to be influenced by the slow mass transfer rate in the beads.

We also conducted the photocatalytic inactivation of *E. coli* by the same CPC reactor with packed GCHBs that was used for contaminant degradation, and no apparent inactivation was achieved in a prolonged reaction time of 24 h (see details in the SD). In contrast, g-C_3N_4 powder was able to inactivate *E. coli* in the slurry reactor, based on our previous study (Shen et al., 2019). *E. coli* is much larger size compared to the chemical contaminants evaluated in the study (sizes 1 − 2 μm (Reshes et al., 2008) vs. 0.65 − 0.86 nm (Lorenc-Grabowska, 2016; Carbamazepine, 2020; Atrazine, 2020; Sulfamethoxazole, 2020)), and thus it was excluded from diffusion into the pores of GCHBs for photocatalytic inactivation. This biological study also demonstrated the diffusion of contaminants played a critical role for their photocatalytic removal.

Another possible explanation for the differences in the observed contaminant degradation kinetics is that the mechanism for contaminant degradation is different. Atrazine and phenol degradation on g-C_3N_4 was systematically evaluated in our previous work, and hole oxidation was believed to play a dominant role for the degradation of these two contaminants (Zheng et al., 2019). During the preparation of GCHBs, embedment of g-C_3N_4 inside the chitosan hydrogel could cover the surface of the photoreactive materials with inert biopolymer, thereby blocking reactive sites and reducing reactivity. Hole oxidation only occurs on the surface of g-C_3N_4, in contrast to the reactive oxygen species (ROS) that could diffuse into the liquid and oxidize contaminants away from the surface. Therefore, the coverage of g-C_3N_4 by chitosan likely has the most negative impact for atrazine and phenol degradation. Our previous study elucidated atrazine adsorption to the g-C_3N_4 played a key role for its reaction kinetics (Zheng et al., 2019), and the reduction of surface binding of atrazine to the photocatalyst

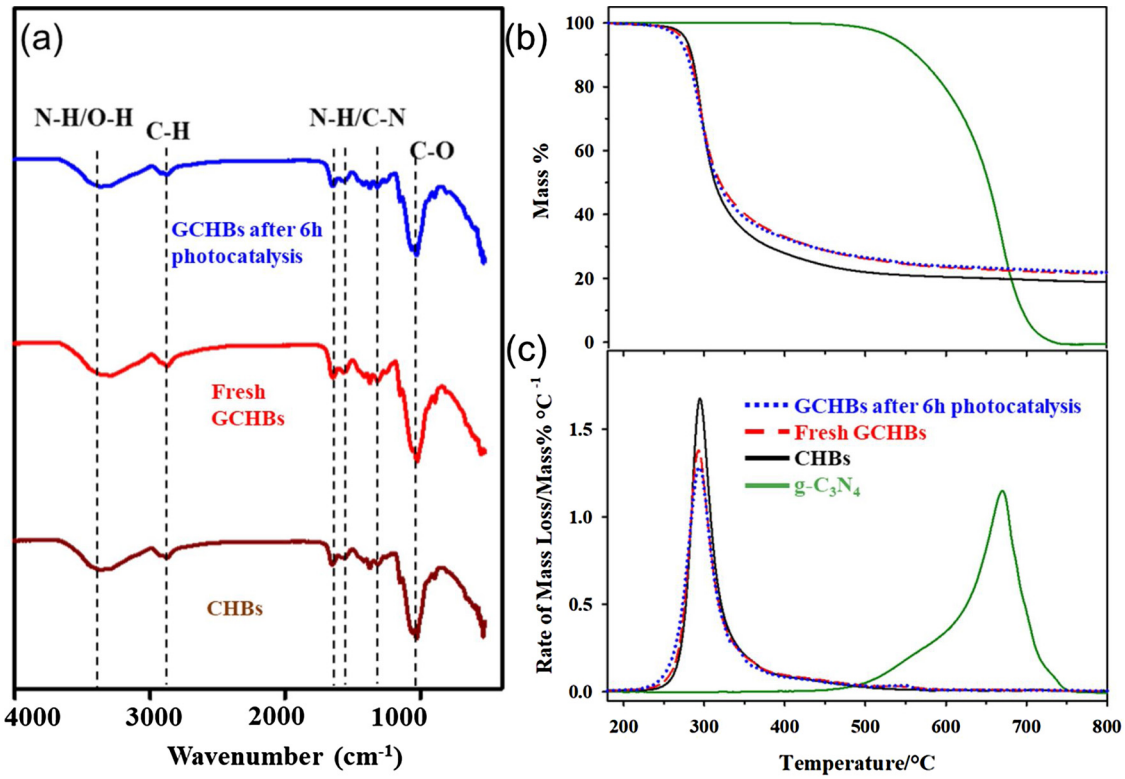

Fig. 4. (a) Attenuated total reflectance-Fourier transform infrared spectroscopy (ATR-FTIR) of CHBs, fresh GCHBs, and GCHBs after 6 h photocatalysis. (b) Thermogravimetric (TG) analysis and (c) derivative thermogravimetric (DTG) analysis of g-C_3N_4, CHBs, fresh GCHBs, and GCHBs after 6 h photocatalysis.

lowers reactivity. Though the CPC reactor has a lower photoreactivity compared to the slurry reactor, it still performs well for degrading some contaminants (i.e., SMZ and CBZ), and it holds promise for pilot-scale or industrial-scale application for water purification because it avoids downstream separating of photocatalysts from the treated water. To further improve the photocatalytic performance, a faster flow rate through the CPC reactor can be used to promote mass transfer, and the immobilization of g-C_3N_4 on the external surface of the chitosan hydrogel beads should be considered in the future.

3.4. Photocatalytic performance in matrices representative of water and wastewater treatment

To evaluate the feasibility and robustness of the CPC reactor packed with GCHBs for pollutant removal in practice, we first tested the phenol degradation kinetics in the real water samples collected from BRWRF and TRWTF, both located in northern Virginia. Samples were collected from the raw water of TRWTF before any treatment (TRWTF-1), the final effluent of TRWTF (TRWTF-2), the effluent after membrane bioreactor treatment in BRWRF (BRWRF-1), and the final effluent of BRWRF (BRWRF-2). As shown in Fig. 5b, little to no inhibition was observed in phenol degradation in most real water samples except for

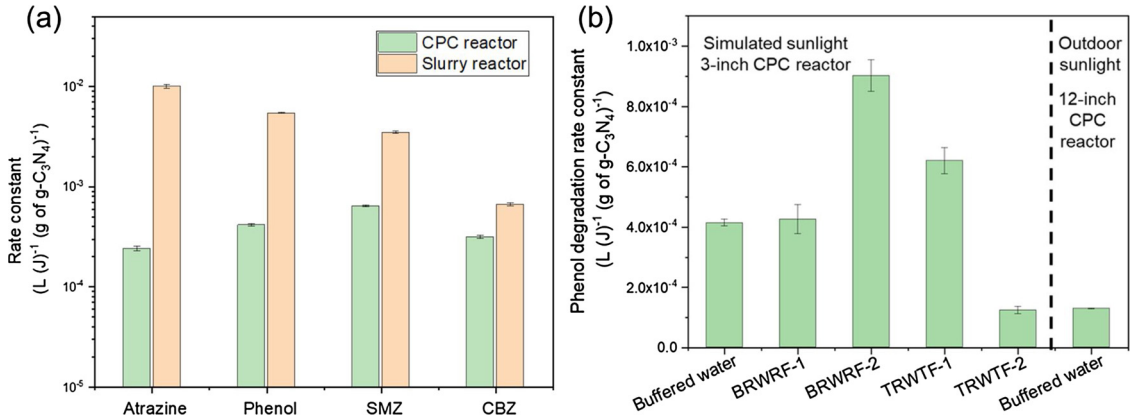

Fig. 5. (a) Photocatalytic degradation rate constants of atrazine, phenol, sulfamethoxazole (SMZ), and carbamazepine (CBZ) in a 3-inch CPC reactor packed with GCHBs and a slurry reactor under simulated sunlight irradiation (1000 W xenon lamp with an AM 1.5 G optical filter). The initial contaminant concentration was 100 μM, and the reactions were conducted in a phosphate buffer (pH 7.3, 1 mM). (b) Photocatalytic degradation rate constants of phenol in a 3-inch CPC reactor under simulated sunlight irradiation and in a 12-inch CPC reactor under outdoor sunlight irradiation. The initial contaminant concentration was 100 μM, and the reactions were conducted in various water samples collected from water and wastewater treatment plants. Error bars represent 95 % confidence intervals derived from regression analysis of a single run.

TRWTF-2. Surprisingly, photocatalytic performance was enhanced in BRWRF-2 and TRWTF-1 by 2.2- and 1.5-fold, respectively, compared to the benchmark reactivity tested in the phosphate buffer. This observation is mostly in agreement with our previous findings that g-C_3N_4 maintained its photoreactivity in complex water matrices that represent water and wastewater treatment practices. Some important water quality parameters could influence bead properties and contaminant-photocatalyst interactions. For example, the ions in the water may not only act as radical scavengers, but also block the active sites on the GCHBs, resulting in the inhibition of photocatalytic reactivity (Farzana and Meenakshi, 2014). The presence of dissolved organic matter (DOM) in natural waters may enhance the photochemical transformation rate of phenol by photolysis (Wenk et al., 2011). Thus, it requires further exploration to understand how complex water matrices tailor the photoreactivity.

3.5. Photocatalytic performance under natural sunlight irradiation

The 3-inch CPC reactor packed with GCHBs was next scaled up to 12 in. (Fig. 1c) and tested under the irradiation of outdoor sunlight (see details in the SD). As shown in Fig. 5b, the phenol degradation rate constant in the 12-inch CPC reactor during the outdoor experiment was slightly smaller to that in the 3-inch CPC reactor under simulated sunlight irradiation in the laboratory (1.3×10^{-4} vs. 4.1×10^{-4} L $(J)^{-1}$ (g of g-$C_3N_4)^{-1}$ for buffered water). The relatively lower phenol degradation kinetics may be due to the temporal change of sunlight intensity and solar zenith angle, which did not allow optimized sunlight harvesting. In contrast, the 3-inch CPC reactor tested in the laboratory allows beams perpendicular to the CPC reactor with maximized sunlight collection and utilization.

3.6. Global drinking water production of the GCHBs/CPC system

To understand the practicality of our photocatalytic system for water treatment, we estimated the capacity of the GCHBs/CPC system for producing high-quality drinking water at a global scale. Based on contaminant degradation kinetics in the 3-inch CPC reactors and global solar intensity, we created a map to highlight the volume of drinking water production per square meter of the reactor per day when 90 % of a contaminant is degraded (Fig. 6, see details in the SD). To reach 90 % removal of atrazine, CBZ, phenol, and SMZ, the reactor can produce 0.6–4.7, 0.8–5.9, 1.0–7.8, and 1.6–12.2 L $(m^2$ of reactor$)^{-1}$ d^{-1} globally, respectively. According to a recent study, 64 countries with less than 80 % rural access to basic drinking water services have significantly greater solar irradiation (5.59 kW h m^{-2} d^{-1}) than the global average (4.70 kW h m^{-2} d^{-1}) (Chu et al., 2019). A 3D printed CPC reactor with a surface area of 3.3 m^2 or 8.8 m^2 (calculated based on SMZ or atrazine degradation kinetics, respectively), which can be installed on the rooftop for a single house (Fig. S4), can generate more than 30 L of drinking water per day in these areas, which is sufficient for daily drinking and food-related water consumption for 4 persons, according to the WHO (Updated WHO/WEDC Technical Notes on WASH in Emergencies, WHO, 2020). We also created a map based on phenol degradation kinetics in 12-inch CPC reactor under outdoor sunlight irradiation (Fig. S5). The results show that the scale-up of CPC reactors could potentially achieve sustainable water treatment in the regions where improved water treatment technologies are most needed. Further advancement of photoreactor design and photocatalytic activity can increase the capacity of drinking water treatment by the CPC reactors.

4. Conclusions

In conclusion, to promote the practicality of photocatalysis for sustainable water treatment, we immobilized g-C_3N_4 on chitosan hydrogel beads and fabricated a scalable CPC photoreactor via 3D printing. The photocatalytic beads (GCHBs) have a 3D mesoporous structure with a high surface area and good mechanical and thermal stability. The CPC reactor with GCHBs showed 2–42-fold smaller rate constants than the slurry reactor for various contaminants degradation, likely due to a reduced mass transfer rate or an inhibited hole-driven photocatalysis. The CPC reactor is still advantageous because it does not require photocatalyst separation after water treatment, and it allows easy handling and reuse of the photocatalyst. Little to no inhibition of photocatalytic reactivity was observed for GCHBs in the real water samples, implying that GCHBs were robust for water purification in the presence of natural water constituents and foulants. Scaling up of a 3-inch laboratory CPC reactor to a 12-inch reactor was also successful

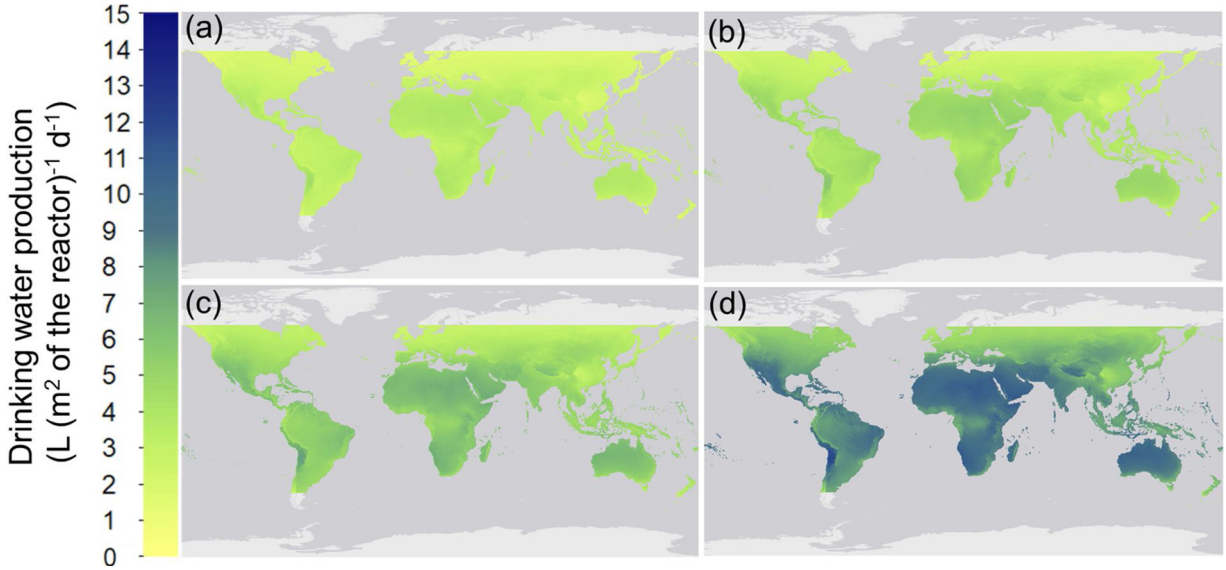

Fig. 6. Global map of drinking water production per surface area of the reactor per day with 90 % removal of (a) atrazine, (b) CBZ, (c) phenol, and (d) SMZ. The data were calculated based on the contaminant degradation kinetics in a 3-inch CPC reactor and the global horizontal irradiance (GHI) of sunlight. The map was created using Esri ArcMap software. Copyright 2019 Esri and its licensors. Data on global horizontal irradiance were obtained from the World Bank (Global Solar Atlas, 2020). GHI data at 30″ resolution between 60 °N and 45 °S were obtained from the Global Solar Atlas. Latitudes outside this range (continents with white background) are not available due to the limitation of satellite imagery accuracy.

for contaminant degradation under sunlight. Moreover, drinking water production capacity was estimated at a global scale, by assuming 90 % removal of contaminants, and a CPC reactor size of 3.3–8.8 m^2 was sufficient to generate sufficient water for family use in most areas where have limited access to basic drinking water service. Our work of CPC reactor design with immobilized photocatalysts presents a step forward in the development of a scalable and sustainable platform for generating high quality potable water by using renewable solar energy.

CRediT authorship contribution statement

Qinmin Zheng: Conceptualization, Methodology, Formal analysis, Writing - original draft, Writing - review & editing, Visualization. **Ashlee Aiello:** Investigation. **Yoon Sil Choi:** Investigation. **Kayla Tarr:** Investigation. **Hongchen Shen:** Investigation. **David P. Durkin:** Investigation, Resources, Writing - original draft, Writing - review & editing, Funding acquisition. **Danmeng Shuai:** Conceptualization, Methodology, Resources, Writing - original draft, Writing - review & editing, Supervision, Project administration, Funding acquisition.

Declaration of Competing Interest

The authors declare that they have no known competing financial interests or personal relationships that could have appeared to influence the work reported in this paper.

Acknowledgements

We acknowledge the Duke Energy Fund at The George Washington University (GW) and NSF CHE-1807617 for supporting the research. We also acknowledge the Air Force Office of Scientific Research (MIPR# F4FGA08354G001) and the United States Naval Academy for facilities support.

Appendix A. Supplementary data

Supplementary material related to this article can be found, in the online version, at doi:https://doi.org/10.1016/j.jhazmat.2020.123097.

References

Antoniou, M.G., Zhao, C., O'Shea, K.E., Zhang, G., Dionysiou, D.D., Zhao, C., Han, C., Nadagouda, M.N., Choi, H., Fotiou, T., Triantis, T.M., Hiskia, A., 2016. Chapter 1: photocatalytic degradation of organic contaminants in water: process optimization and degradation pathways. Photocatalysis 1–34. https://doi.org/10.1039/9781782627104-00001.

Atrazine, https://pubchem.ncbi.nlm.nih.gov/compound/2256 (Accessed October 27, 2019).

Benotti, M.J., Stanford, B.D., Wert, E.C., Snyder, S.A., 2009. Evaluation of a photocatalytic reactor membrane pilot system for the removal of pharmaceuticals and endocrine disrupting compounds from water. Water Res. 43, 1513–1522. https://doi.org/10.1016/j.watres.2008.12.049.

Blanco, J., Malato, S., Fernández, P., Vidal, A., Morales, A., Trincado, P., Oliveira, J.C., Minero, C., Musci, M., Casalle, C., Brunotte, M., Tratzky, S., Dischinger, N., Funken, K.-H., Sattler, C., Vincent, M., Collares-Pereira, M., Mendes, J.F., Rangel, C.M., 1999. Compound parabolic concentrator technology development to commercial solar detoxification applications. Sol. Energy 67, 317–330. https://doi.org/10.1016/S0038-092X(00)00078-5.

Braham, R.J., Harris, A.T., 2009. Review of major design and scale-up considerations for solar photocatalytic reactors. Ind. Eng. Chem. Res. 48, 8890–8905. https://doi.org/10.1021/ie900859z.

Brame, J., Long, M., Li, Q., Alvarez, P., 2014. Trading oxidation power for efficiency: differential inhibition of photo-generated hydroxyl radicals versus singlet oxygen. Water Res. 60, 259–266. https://doi.org/10.1016/j.watres.2014.05.005.

Brame, J., Long, M., Li, Q., Alvarez, P., 2015. Inhibitory effect of natural organic matter or other background constituents on photocatalytic advanced oxidation processes: mechanistic model development and validation. Water Res. 84, 362. https://doi.org/10.1016/j.watres.2015.07.044.

Cao, S., Low, J., Yu, J., Jaroniec, M., 2015. Polymeric photocatalysts based on graphitic carbon nitride. Adv. Mater. 27, 2150–2176. https://doi.org/10.1002/adma.201500033.

Carbamazepine, https://pubchem.ncbi.nlm.nih.gov/compound/2554 (Accessed October 27, 2019).

Chiou, M.S., Li, H.Y., 2003. Adsorption behavior of reactive dye in aqueous solution on chemical cross-linked chitosan beads. Chemosphere 50, 1095–1105. https://doi.org/10.1016/S0045-6535(02)00636-7.

Chong, M.N., Jin, B., Chow, C.W.K., Saint, C., 2010. Recent developments in photocatalytic water treatment technology: a review. Water Res. 44, 2997–3027. https://doi.org/10.1016/j.watres.2010.02.039.

Chu, C., Ryberg, E.C., Loeb, S.K., Suh, M.-J., Kim, J.-H., 2019. Water disinfection in rural areas demands unconventional solar technologies. Acc. Chem. Res. 52, 1187–1195. https://doi.org/10.1021/acs.accounts.8b00578.

Colina-Márquez, J., Machuca-Martínez, F., Li Puma, G., 2009. Photocatalytic mineralization of commercial herbicides in a pilot-scale solar CPC reactor: photoreactor modeling and reaction kinetics constants independent of radiation field. Environ. Sci. Technol. 43, 8953–8960. https://doi.org/10.1021/es902004b.

Colina-Márquez, J., Machuca-Martínez, F., Puma, G.L., 2010. Radiation absorption and optimization of solar photocatalytic reactors for environmental applications. Environ. Sci. Technol. 44, 5112–5120. https://doi.org/10.1021/es100130h.

Dal Pozzo, A., Donzelli, G., Rodriquez, L., Tajana, A., 1989. "In vitro" model for the evaluation of drug distribution and plasma protein-binding relationships. Int. J. Pharm. 50, 97–101. https://doi.org/10.1016/0378-5173(89)90133-6.

Dong, F., Wang, Z., Li, Y., Ho, W.-K., Lee, S.C., 2014. Immobilization of polymeric g-C_3N_4 on structured ceramic foam for efficient visible light photocatalytic air purification with real indoor illumination. Environ. Sci. Technol. 48, 10345–10353. https://doi.org/10.1021/es502290f.

Dong, Q., Mohamad Latiff, N., Mazánek, V., Rosli, N.F., Chia, H.L., Sofer, Z., Pumera, M., 2018. Triazine- and heptazine-based carbon nitrides: toxicity. ACS Appl. Nano Mater. 1, 4442–4449. https://doi.org/10.1021/acsanm.8b00708.

Farzana, M.H., Meenakshi, S., 2014. Photo-decolorization and detoxification of toxic dyes using titanium dioxide impregnated chitosan beads. Int. J. Biol. Macromol. 70, 420–426. https://doi.org/10.1016/j.ijbiomac.2014.07.021.

Global Solar Atlas, https://globalsolaratlas.info/map?c=11.523088,8.173828,3 (Accessed November 8, 2019).

Haag, W.R., Yao, C.C.D., 1992. Rate constants for reaction of hydroxyl radicals with several drinking water contaminants. Environ. Sci. Technol. 26, 1005–1013. https://doi.org/10.1021/es00029a021.

Hoekman, D., Hansch, C.H., Leo, A., 1995. Exploring QSAR: Hydrophobic, Electronic, and Steric Constants 2. https://books.google.com/books?id=8c7dMwEACAAJ.

Hoffmann, M.R., Martin, S.T., Choi, W.Y., Bahnemann, D.W., 1995. Environmental applications of semiconductor photocatalysis. Chem. Rev. 95, 69. https://doi.org/10.1021/cr00033a004.

Hong, P.-Z., Li, S.-D., Ou, C.-Y., Li, C.-P., Yang, L., Zhang, C.-H., 2007. Thermogravimetric analysis of chitosan. J. Appl. Polym. Sci. 105, 547–551. https://doi.org/10.1002/app.25920.

Hu, C., Lin, Y.-R., Yang, H.-C., 2019. Recent developments in graphitic carbon nitride based hydrogels as photocatalysts. ChemSusChem 12, 1794–1806. https://doi.org/10.1002/cssc.201802257.

Jiang, W., Luo, W., Zong, R., Yao, W., Li, Z., Zhu, Y., 2016. Polyaniline/carbon nitride nanosheets composite hydrogel: a separation-free and high-efficient photocatalyst with 3D hierarchical structure. Small 12, 4370–4378. https://doi.org/10.1002/smll.201601546.

Keane, D.A., McGuigan, K.G., Fernández Ibáñez, P., Inmaculada Polo-López, M., Anthony Byrne, J., Dunlop, P.S.M., O'Shea, K., Dionysiou, D.D., Pillai, S.C., 2014. Solar photocatalysis for water disinfection: materials and reactor design. Catal. Sci. Technol. 4, 1211–1226. https://doi.org/10.1039/C4CY00006D.

Kumirska, J., Czerwicka, M., Kaczyński, Z., Bychowska, A., Brzozowski, K., Thöming, J., Stepnowski, P., 2010. Application of spectroscopic methods for structural analysis of chitin and chitosan. Mar. Drugs 8, 1567–1636. https://doi.org/10.3390/md8051567.

Loeb, S.K., Alvarez, P.J.J., Brame, J.A., Cates, E.L., Choi, W., Crittenden, J., Dionysiou, D.D., Li, Q., Li-Puma, G., Quan, X., Sedlak, D.L., David Waite, T., Westerhoff, P., Kim, J.-H., 2018. The technology horizon for photocatalytic water treatment: sunrise or sunset? Environ. Sci. Technol. https://doi.org/10.1021/acs.est.8b05041.

Lorenc-Grabowska, E., 2016. Effect of micropore size distribution on phenol adsorption on steam activated carbons. Adsorption 22, 599–607. https://doi.org/10.1007/s10450-015-9737-x.

McCullagh, C., Skillen, N., Adams, M., Robertson, P.K., 2011. Photocatalytic reactors for environmental remediation: a review. J. Chem. Technol. Biotechnol. 86, 1002–1017. https://doi.org/10.1002/jctb.2650effec.

Miranda-García, N., Suárez, S., Sánchez, B., Coronado, J.M., Malato, S., Maldonado, M.I., 2011. Photocatalytic degradation of emerging contaminants in municipal wastewater treatment plant effluents using immobilized TiO_2 in a solar pilot plant. Appl. Catal. B Environ. 103, 294–301. https://doi.org/10.1016/j.apcatb.2011.01.030.

Moreira, N.F.F., Sampaio, M.J., Ribeiro, A.R., Silva, C.G., Faria, J.L., Silva, A.M.T., 2019. Metal-free g-C_3N_4 photocatalysis of organic micropollutants in urban wastewater under visible light. Appl. Catal. B Environ. 248, 184–192. https://doi.org/10.1016/j.apcatb.2019.02.001.

Navntoft, C., Araujo, P., Litter, M.I., Apella, M.C., Fernández, D., Puchulu, M.E., del V. Hidalgo, M., Blesa, M.A., 2006. Field tests of the solar water detoxification SOLWATER reactor in Los Pereyra, Tucumán, Argentina. J. Sol. Energy Eng. 129, 127–134. https://doi.org/10.1115/1.2391318.

Neta, P., Dorfman, L.M., 1968. Pulse radiolysis studies. XIII. Rate constants for the reaction of hydroxyl radicals with aromatic compounds in aqueous solutions. Radiat. Chem. American Chemical Society, pp. 222–230. https://doi.org/10.1021/ba-1968-0081.ch015.

Niu, P., Zhang, L., Liu, G., Cheng, H., 2012. Graphene-like carbon nitride nanosheets for improved photocatalytic activities. Adv. Funct. Mater. 22, 4763. https://doi.org/10.1002/adfm.201200922.

Ong, W.-J., Tan, L.-L., Ng, Y.H., Yong, S.-T., Chai, S.-P., 2016. Graphitic carbon nitride (g-

C_3N_4)-based photocatalysts for artificial photosynthesis and environmental remediation: are we a step closer to achieving sustainability? Chem. Rev. 116, 7159–7329. https://doi.org/10.1021/acs.chemrev.6b00075.

Oulton, R.L., Kohn, T., Cwiertny, D.M., 2010. Pharmaceuticals and personal care products in effluent matrices: a survey of transformation and removal during wastewater treatment and implications for wastewater management. J. Environ. Monit. 12, 1956–1978. https://doi.org/10.1039/C0EM00068J.

Polo-López, M.I., Fernández-Ibáñez, P., García-Fernández, I., Oller, I., Salgado-Tránsito, I., Sichel, C., 2010. Resistance of *Fusarium sp* spores to solar TiO_2 photocatalysis: influence of spore type and water (scaling-up results). J. Chem. Technol. Biotechnol. 85, 1038–1048. https://doi.org/10.1002/jctb.2397.

Ramos, B., Couri, A.P., Ookawara, S., Teixeira, A.C.S.C., 2019. Micro-structured packed bed reactors for solar photocatalysis: impacts of packing size and material on light harnessing. Photochem. Photobiol. Sci. 18, 577–582. https://doi.org/10.1039/C8PP00371H.

Raulio, M., Pore, V., Areva, S., Ritala, M., Leskelä, M., Lindén, M., Rosenholm, J.B., Lounatmaa, K., Salkinoja-Salonen, M., 2006. Destruction of deinococcus geothermalis biofilm by photocatalytic ALD and sol-gel TiO_2 surfaces. J. Ind. Microbiol. Biotechnol. 33, 261–268. https://doi.org/10.1007/s10295-005-0063-2.

Reshes, G., Vanounou, S., Fishov, I., Feingold, M., 2008. Cell shape dynamics in escherichia coli. Biophys. J. 94, 251–264. https://doi.org/10.1529/biophysj.107.104398.

Shen, H., López-Guerra, E.A., Zhu, R., Diba, T., Zheng, Q., Solares, S.D., Zara, J.M., Shuai, D., Shen, Y., 2019. Visible-light-responsive photocatalyst of graphitic carbon nitride for pathogenic biofilm control. ACS Appl. Mater. Interfaces 11, 373–384. https://doi.org/10.1021/acsami.8b18543.

Sichel, C., Tello, J., de Cara, M., Fernández-Ibáñez, P., 2007. Effect of UV solar intensity and dose on the photocatalytic disinfection of bacteria and fungi. Catal. Today 129, 152–160. https://doi.org/10.1016/j.cattod.2007.06.061.

Spasiano, D., Marotta, R., Malato, S., Fernandez-Ibañez, P., Di Somma, I., 2015. Solar photocatalysis: materials, reactors, some commercial, and pre-industrialized applications. A comprehensive approach. Appl. Catal. B Environ. 170–171, 90–123. https://doi.org/10.1016/j.apcatb.2014.12.050.

Sulfamethoxazole, https://pubchem.ncbi.nlm.nih.gov/compound/Sulfamethoxazole (Accessed October 27, 2019).

Sun, J., Schmidt, B.V.K.J., Wang, X., Shalom, M., 2017. Self-standing carbon nitride-based hydrogels with high photocatalytic activity. ACS Appl. Mater. Interfaces 9, 2029–2034. https://doi.org/10.1021/acsami.6b14879.

Updated WHO/WEDC Technical Notes on WASH in Emergencies, WHO. http://www.who.int/water_sanitation_health/publications/technotes/en/ (Accessed November 8, 2019).

Wenk, J., von Gunten, U., Canonica, S., 2011. Effect of dissolved organic matter on the transformation of contaminants induced by excited triplet states and the hydroxyl radical. Environ. Sci. Technol. 45, 1334–1340. https://doi.org/10.1021/es102212t.

Xiao, J., Han, Q., Xie, Y., Yang, J., Su, Q., Chen, Y., Cao, H., 2017. Is C_3N_4 chemically stable toward reactive oxygen species in sunlight-driven water treatment? Environ. Sci. Technol. 51, 13380–13387. https://doi.org/10.1021/acs.est.7b04215.

Yu, Q., Deng, S., Yu, G., 2008. Selective removal of perfluorooctane sulfonate from aqueous solution using chitosan-based molecularly imprinted polymer adsorbents. Water Res. 42, 3089–3097. https://doi.org/10.1016/j.watres.2008.02.024.

Zhang, M., Jiang, W., Liu, D., Wang, J., Liu, Y., Zhu, Y., Zhu, Y., 2016. Photodegradation of phenol via C_3N_4-agar hybrid hydrogel 3D photocatalysts with free separation. Appl. Catal. B Environ. 183, 263–268. https://doi.org/10.1016/j.apcatb.2015.10.049.

Zhao, C., Yan, Q., Wang, S., Dong, P., Zhang, L., 2018. Regenerable g-C_3N_4–chitosan beads with enhanced photocatalytic activity and stability. RSC Adv. 8, 27516–27524. https://doi.org/10.1039/C8RA04293D.

Zheng, Q., Durkin, D.P., Elenewski, J.E., Sun, Y., Banek, N.A., Hua, L., Chen, H., Wagner, M.J., Zhang, W., Shuai, D., 2016. Visible-light-responsive graphitic carbon nitride: rational design and photocatalytic applications for water treatment. Environ. Sci. Technol. 50, 12938–12948. https://doi.org/10.1021/acs.est.6b02579.

Zheng, Q., Shen, H., Shuai, D., 2017. Emerging investigators series: advances and challenges of graphitic carbon nitride as a visible-light-responsive photocatalyst for sustainable water purification. Environ. Sci. Water Res. Technol. 3, 982–1001. https://doi.org/10.1039/C7EW00159B.

Zheng, Q., Xu, E., Park, E., Chen, H., Shuai, D., 2019. Looking at the overlooked hole oxidation: photocatalytic transformation of organic contaminants on graphitic carbon nitride under visible light irradiation. Appl. Catal. B Environ. 240, 262–269. https://doi.org/10.1016/j.apcatb.2018.09.012.